Evaluation of fatigue damage of a railhead using an indentation test, acoustic methods and microstructural observations

Stanisław Kucharski [*], Sławomir Mackiewicz, Tomasz Katz, Grzegorz Starzyński, Zbigniew Ranachowski, Stefania Woźniacka

Institute of Fundamental Technological Research, Warsaw, Poland

ABSTRACT

The paper presents an investigation of the railhead steel R260. Brinell hardness was measured, spherical microindentation tests were performed and the microstructure was analysed using optical microscopy and SEM images. Fatigue damage in various near-surface regions of the railhead was estimated on the basis of local deterioration of elastic modulus and the development of plastic work in cyclic microindentation tests. There is a clear difference in hardness and fatigue damage between the used and the virgin regions of the railhead. The Brinell hardness and ultrasonic measurements show a change in material properties due to rail manufacturing process.

1. Introduction

Railway rails are usually made of high-carbon steel with a pearlitic structure. Steels of this type are characterized by high strength and hardness and high abrasion resistance, as well as low ductility and lowered fracture toughness. Materials with a pearlitic structure owe their high abrasion resistance to their microstructure, which consists of hard cementite plates in a soft ferritic matrix [1]. The strength of pearlitic steels is associated with a Hall–Petch type relationship with respect to the interlamellar spacing [2,3]. This is explained by a dislocation pile-up model that restricts the dislocation mobility. Precise simulations of the dependence of hardness on the interlamellar spacing are presented in [4]. Three parameters describe the microstructure of pearlitic steels: grain size, pearlite colony size and interlamellar spacing. The authors of paper [4] have experimentally verified the analytical relationship between hardness and interlamellar spacing, and have shown that increasing the interlamellar spacing from 0.1 μm to 0.2 μm causes a 15% reduction in the hardness of the steel.

Early studies of rails [5] (presented in an article published in 1982) showed the existence of a surface layer of increased hardness related to the plastic hardening of the deformed material at the surface, as well as much greater hardening in the formation of corrugation peaks (skid waves).

Complex load conditions exist in a rail transport system that alter the microstructure of the material of the wheels and rails near the contact area [6]. This paper presents a microstructure and hardness study of virgin and used pearlitic rail steel. The samples were prepared from the railhead section. The microstructure images for the primary rail sample and the used rail were taken from the middle and corner sections. Microstructural observations indicated the existence of proeutectoid ferrite at the grain boundaries for the sample near the rail surface. The presence of this modified material promotes the initiation of micro-cracks, resulting in the formation of abrasive debris and rolling contact fatigue defects. The Vickers hardness test method was used to obtained the hardness profile of the material and was carried out for both the used and the virgin rail steel at a distance of 0.3 mm, 0.6 mm and 0.9 mm from the surface along the depth. The results show an increase of approximately 10% in the hardness value of the material close to the surface, while the hardness of the base material remained almost the same. Higher surface Vickers hardness values indicate the formation of a brittle material that is more prone to crack initiation and propagation.

Paper [7] presents Finite Element simulation of microstructural changes in the wheel–rail contact area. R350HT steel was used in the investigation. The simulation results show that the temperature on the rail track reaches 1200 °C, and that at a depth of 100 μm the temperature drops to 200 °C. The entire heating and cooling process takes less than 1 ms. This means that, during each wheel–rail contact and heating process, austenite can be formed. Moreover, at the cooling rates that occur, the austenite that forms at the elevated temperatures has no time to convert back to pearlite on cooling but is either hardened as austenite or

---

* Corresponding author.
  E-mail address: skuchar@ippt.pan.pl (S. Kucharski).

converted to martensite. The authors also present the stress distribution under the train wheel which allows them to draw conclusions about the plastic deformation as a function of depth. The highest von Mises stresses of about 800 MPa are achieved in the wheel–railhead contact area, and are higher than the yield point of undeformed steel of the type being investigated, which is 750 MPa. Accordingly, the rail deforms plastically upon wheel–rail contact to a depth of at least 200 μm. However, the yield point is a macroscopic property of the material, and grains oriented towards slippage will also deform in deeper areas. At the same time, the yield strength of steel decreases with increasing temperature. Hence, the calculated von Mises stress levels represent the lower limit of the plastic deformation at high temperatures in the wheel–rail area.

Similar results are obtained in [8]. In this paper, solutions based on the analysis of a two-dimensional thermomechanical elastic–plastic finite element are provided to examine the effect of heat generated at the dynamic wheel–rail contact interface. Surface temperatures of several hundred degrees Celsius were observed, but heat penetration below the surface was shallow and the thermal gradients were steep. This promotes the microstructural transformation of the rail material to martensite in the vicinity of the surface.

Although the hardness was often measured to estimate the mechanical properties of the rails, it was rarely used to evaluate their fatigue damage. However there are many papers, presented in the review by Bjoerheim et al. [9], about the correlation between the evolution of the damage in fatigue test and the change in hardness for metals. It can be seen, that this correlation was observed many years ago, [10,11,12]. The authors of [11,12] found that the Vickers hardness measured at different stages of fatigue test depends on cyclic hardening/softening effect, similarly to post cycled tensile curve. They showed that for steel (pearlite and ferrite phases) the micro-hardness does not change monotonically with number of loading cycles, but initially increases, then decreases.

For Al-2024-T42 alloy, in which the micro-hardness continuously increases with number of cycles, the model of fatigue damage estimation, based on hardness evolution during fatigue test was analysed, and damage function was derived depending on stress amplitude and number of cycles [13].

The Vickers microhardness evolution during fatigue test was used to define the damage variable, [14], that can be a measure of the fatigue damage. Damage criterion, based on instrumented indentation test was proposed to predict the fatigue life of cyclically loaded steel structures, [15]. The authors observed that for samples submitted to fatigue loads, there is a difference in change in microhardness between as received and annealed conditions.

Detection of fatigue damage level by measuring the hardness was also performed by Miroslav et al., [16]. They show that for 24CrMoV55 steel, and for high stress amplitude the hardness continuously decreases, with number of cycles, and this tendency slightly changes for higher stress amplitude, i.e. after the decrease begin to increase. For S355J0 steel there was an inverse tendency, the hardness initially increases then decreases for all applied stress amplitudes. This evolution of hardness corresponds to behavior of respective steels under cyclic loading i.e. cyclic softening and cyclic hardening.

The use of ultrasonic methods to detect fatigue defects is difficult because usually the average defects diameters are shorter than the ultrasonic wavelengths [17], and the nonlinear ultrasonic method is used to solve this problem [18]. In another approach, the sensitivity of ultrasonic waves to dislocation density was used and the method was applied to rail steel [19].

The objective of this study was to explore the effects of the contact load applied during the service life of the railhead. We examined the surface and the cross-section of the railhead. At the macro scale the Brinell hardness and the elastic modulus (using an ultrasonic method) were measured. At the micro scale, micro-indentation tests with spherical tip were used to capture the local values of the indentation hardness

and elastic modulus. Additionally, we conducted cyclic micro-indentation tests. A decrease in elastic modulus E, and a change in the evolution of the hysteresis loops in the cyclic test can be associated with the local fatigue damage of the material.

2. Experiment

In this paper, we chose spherical indentation to measure hardness, since spherical indenters do not generate the large concentration of stress that is present in a sharp indentation (Vickers, Berkovich). Therefore, the results for the spherical indentation may be better correlated with the yield stress. Macro hardness tests (the Brinell hardness test) and spherical micro-indentation tests were therefore performed on the rail. At the macro scale (for the Brinell test), a ball of diameter 2.5 mm and a load of 1839.4 N were used. The hardness was specified using the classical method: after unloading, the diameter d of the residual impression was measured using an optical microscope (Olympus DSX 510), and the hardness was calculated using the formula.

$$\text{HB} = \frac{2*0.102*P}{\pi*D*\left(D - \sqrt{D^2 - d^2}\right)} \left[\frac{\text{kgf}}{\text{mm}^2}\right] \tag{1}$$

where D is the ball diameter, [mm], and P the loading force, [N].

Taking into account the residual impression diameter (0.8–0.9 mm), the minimal distance from the railhead surface (the sample boundary on the cross-section) should be no less than 4–5 mm. Therefore the Brinell hardness was additionally measured with a 0.5 mm diameter ball (micro-indentation) under a load of 29.9 N, which enabled us to perform the indentation closer to the sample boundary.

The micro-indentation tests described here were carried out with a spherical tip having a nominal radius 50 μm under a load of 7.2 N, which corresponds to a residual imprint of approximately 6 μm depth. The microhardness (indentation hardness, HIT) was specified from an analysis of the indentation unloading curve using the generally accepted Oliver–Pharr method, and the latter was also used to calculate the elastic modulus.

In our study we distinguish the two sides of the railhead. The "used" or "hardened" side is located on the inside of the railway track, which is cyclically loaded by the wheel. The "unused" or "non-hardened" railhead side is located on the outside of the railway track, which is not directly touched by the wheel and holds its initial shape and microstructure. This side we call the virgin side.

3. Results

3.1. Mechanical properties
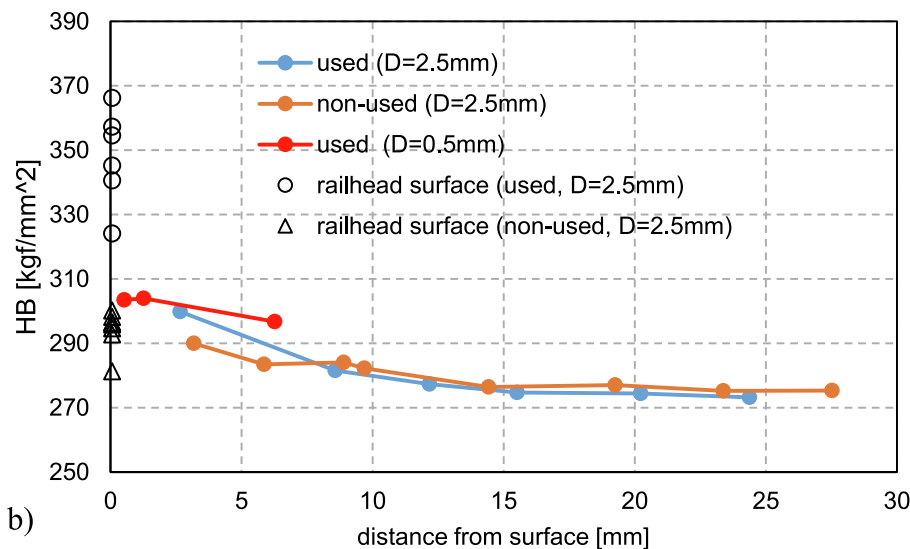
3.1.1. Brinell hardness

The Brinell (macro) hardness was determined along paths taking two directions: the first on the surface of the railhead, along the direction of wheel motion, and the second on a cross-section of the railhead, along the depth from the head surface (see Fig. 1a). The latter path is about 30 mm long. Both the used and the unused side of the railhead were examined.

On the used side, on the head surface, we observe a scattering of results (the Brinell hardness varied between 320 and 366 with a mean value equal to 348), while on the unused side the hardness was lower and had a mean value equal to 294, and a lower scattering of results was observed. This indicates that the rail surface hardens as a result of the contact load imposed by the wheel. The results for the cross-section and the head surface are presented in Fig. 1b.

The hardness decreases with the distance from the surface, on both the used and the unused side of the railhead. This is a result of rolling in the rail manufacturing process. Nevertheless, in the region closer to the rail surface (<7 mm), the hardness is greater on the used side than on the unused side. This gives confirmation of the material hardening detected
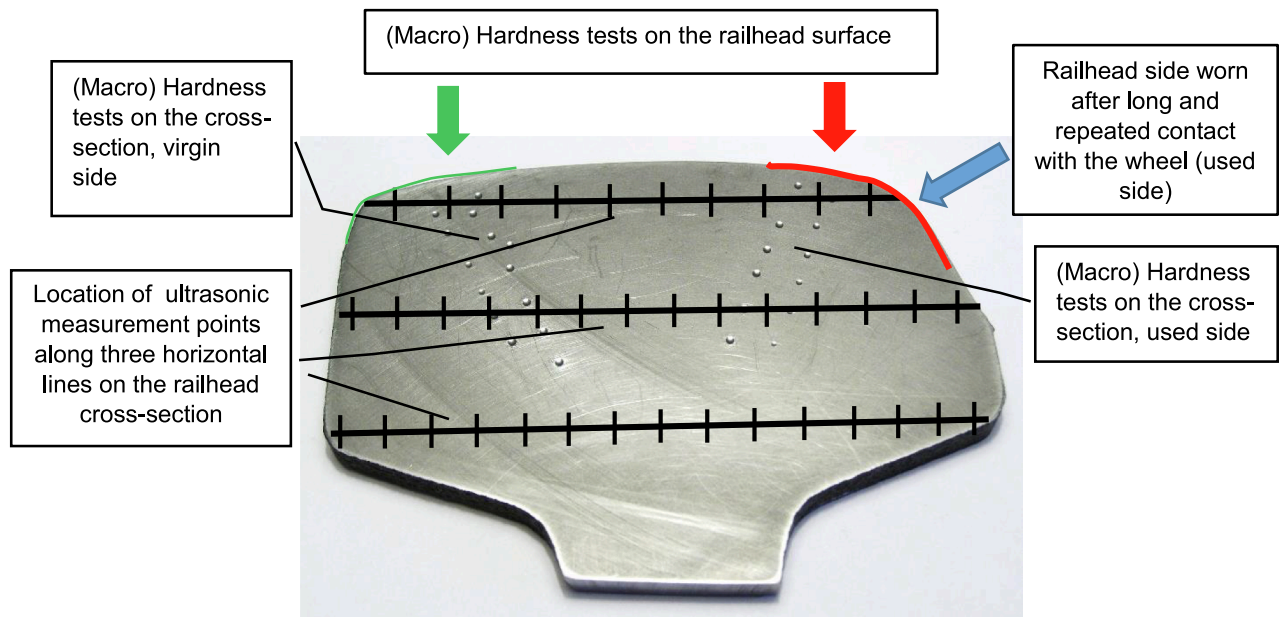
Fig. 1. a) location of hardness and ultrasonic measurements on railhead cross-section; b) Brinell hardness measured with different balls (D = 2.5 mm and D = 0.5 mm) on the cross-section of railhead (used and non-used side). Brinell hardness measurements of railhead surface are presented as separate points, at the beginning of the horizontal axis.

by the Brinell test on the rail surface on the used side. In order to determine the Brinell hardness on this side at smaller distances (i.e. 0.5–1 mm from the rail surface), a tip with a smaller radius, R = 50 μm was used. However, the maximum value (306) measured on the cross-section (close to the surface) was still lower than the mean value found on the rail surface (348), Fig. 1. It is worth noting that the measurement of Brinell hardness performed on the cross-section with completely different balls gave similar results.

The difference in Brinell hardness measured on the rail cross-section and the rail surface may result from the fact that residual stress (generated at the surface by the contact load) affects the indentation test at the railhead surface and the railhead cross-section in different ways (in the latter the residual stress is probably realized after sample cutting).

On the unused side the maximum value measured on the cross-section (290), even at a few millimetres from the surface, was close to

that specified on the rail surface.

3.1.2. Indentation hardness (HIT)

Multiple micro-hardness tests with a recording of the load-penetration curve were performed on the cross-section of railhead. In the tests, the indentation hardness (*HIT*) and the elastic modulus, *E* were determined using the Oliver–Pharr method. The small diameter of the residual imprints (≈50 μm) enabled us to examine the regions close to the railhead surface thoroughly.

Both the unused and the used side of the rail were investigated. Beneath the surface of the latter, sub-surface cracks are formed that can be the start of the stripping of a thin layer of rail material from the surface. These cracks were visible on the cross-section. Micro-indentation tests were also performed in the vicinity of the cracks to clarify whether the local material properties influence the crack evolution.

On the unused side, the micro-indentation tests were arranged on

grid (matrix), M_{un} (11X2 indents). Additionally, some tests were performed on both sides of the grid, close to the rail surface, Fig. 2. The results for the indentation hardness and elastic modulus are shown in Fig. 3. For the area covered by the grid, the values of E vary randomly with the distance from the rail surface, and a scattering of results is visible, but in general the elastic modulus does not increase or decrease continuously. The values of E at the points located outside the grid, Fig. 2, near the rail surface, are presented as separate points in Fig. 3a. The mean value for all the measurements is close to 212 GPa, which is a standard value for R260 steel.

A similar tendency can be observed for the hardness measurements. A scattering of results is also visible, but we can say that the hardness is practically unchanged with distance from the surface, Fig. 3b, for the unused side.

On the used side, the state of the material is much more complex because of the cyclic contact load. To show the change in the material properties with the distance from the rail surface, three regular matrices of indents were made: two matrices M1 and M2 (3X7 indentations), and one matrix M3 (2X11 indentations) (see Fig. 4). Additionally, the indentation tests were carried out at some characteristic points to capture the properties of the sub-surface regions of the rail that were damaged by the contact load.

The results for the elastic modulus and hardness measurements for the matrices are presented in Fig. 5 as a function of distance from the surface. Each point in the diagrams corresponds to a mean of three (for M1, M2) or two (M3) measurements. The following observations can be made from Fig. 5. In all cases, the elastic modulus shows its smallest values near the rail surface, and increases with distance from the surface. The lowest values of E are found in the matrix M3 since this starts at the smallest distance from the sample surface. When the distance from surface is greater than 1000 μm, the values of the elastic modulus are similar for the matrices M1 and M2, and these are slightly higher than the values for the matrix M3.

The change of the indentation hardness exhibits an inverse tendency: HIT decreases with distance from the surface. The values for HIT are similar for matrices M1 and M2, although the hardness in the M2 region is slightly greater. This can be attributed to the greater hardening in this region, since M2 is located in the vicinity of the tip of a long crack.

The greater hardness in the regions located closer to the rail surface

indicates that plastic deformation takes place in the railhead during the contact with the wheel and that the material hardens, but the mechanism for this hardening is not evident. It should be noted that the hardness after strain hardening should be approximately three times the maximum yield stress. Since the latter (after strain hardening) equals about 1000 MPa for R260 steel, the corresponding hardness should be approximately 3000 MPa. This value is registered in points located far from the rail surface, but in the sub-surface region the measured hardness reaches ~4400 MPa. This high value cannot be explained by simple strain hardening, and may be attributed to structural changes in the severely deformed railhead regions.

Micro-indentation tests were also carried out near a crack that starts from the surface, to capture the material properties in the crack region (see Fig. 6). The results (hardness and elastic modulus) for some of these tests are shown just by impressions in Fig. 6a,b. Some tests were also performed along the rail surface (red line), or along the crack (blue line), and the corresponding results are presented in Fig. 7. At these points the elastic modulus fluctuated at around 160 MPa; this value is lower than that measured in the matrix region (Fig. 5a). The lowest values of E, observed at points near the surface and near the crack, indicate that the fatigue damage is most advanced at these points. The hardness at all points is higher than that measured in the part of the matrix that is located at a greater distance from the rail surface, and is slightly lower at points located along the crack than at points close to the surface. This indicates that at the latter points the hardening effect is more advanced, because of the higher stress resulting from the contact load. The presence of the crack means that the hardness along the crack at the points located below the crack (blue line) does not change with distance (i.e. it is stable even though the distance from the surface increases).

The remaining indents are randomly located near the rail surface or near the crack, so the values for the hardness and the elastic modulus are written next to the indentation points in Fig. 6. The scattering of the results can be attributed to the small-scale indentation (the residual impression diameter is approximately 50 μm): at this scale, the examined steel is not perfectly homogeneous. These results confirm the previous observations (Figs. 4-6) that the elastic modulus decreases in the area located near the rail surface, while at the same time the hardness increases. It can be seen that in the specific region between the crack and the rail surface, the values for the hardness and E fluctuate around the corresponding values and do not depend on the distance from the surface. This indicates that in this region we have almost a homogeneous degree of damage and hardening. Moreover, there is a distinct difference in the values for HIT and E between the regions located above and below the crack.

The results for the indentation test in the vicinity of a short crack are presented in Fig. 8.

3.2. Microstructural observations

3.2.1. Characterization with optical microscopy

The changes in the mechanical properties (elastic modulus, micro- and macro-hardness) examined above can be correlated with the microstructure of the railhead. On the basis of the observation of the microstructure of the material, two characteristic areas can be distinguished on the cross-section of the used side of the railhead. The first is the region most affected by the contact load (denoted by A in Fig. 9), which is located directly beneath the railhead surface (see Fig. 9). This is a layer composed of the material that is most deformed as a result of the contact with the wheel. The thickness of the layer is not constant. In this region the phases are difficult to recognize and the grains are finer. The remaining part of the material that is located below the layer is denoted as region B. The microstructure in area B is similar to that observed in the unused part of the railhead: the different phases are visible, and the shape and size of the grains are the same as in the virgin, "as received", material. There is no distinct boundary between region A and region B: a continuous change in the microstructure is observed between the
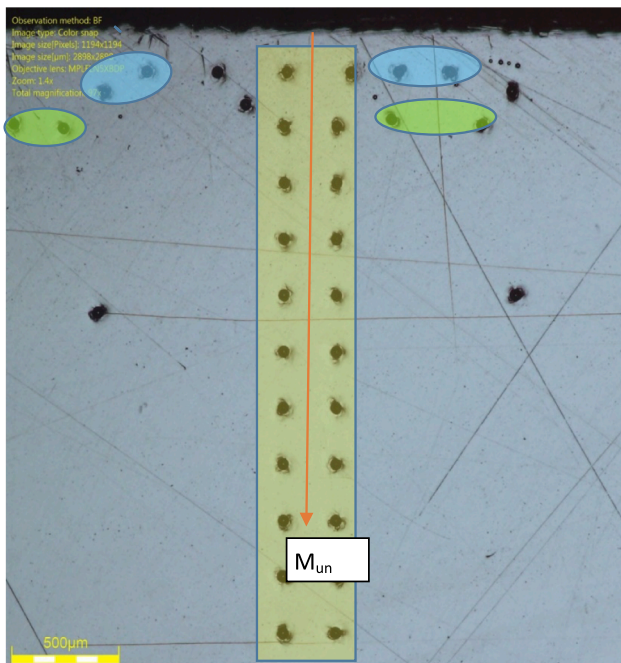

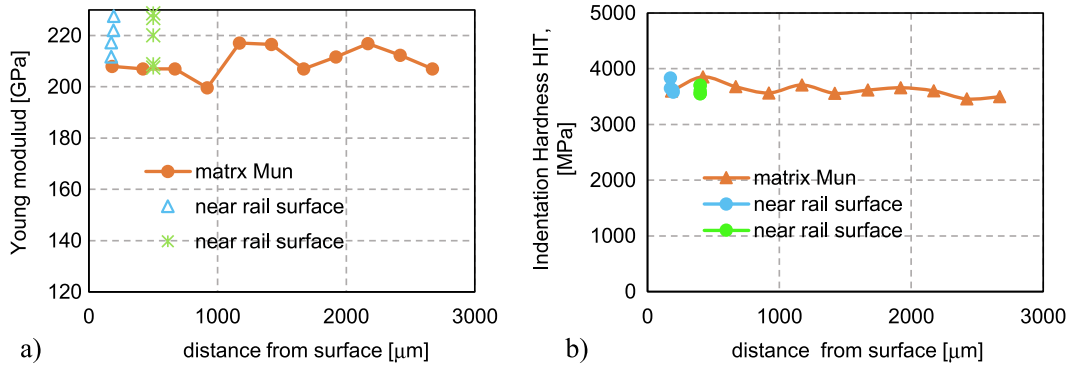**Fig. 2.** Location of indents on cross-section. Unused side.

Fig. 3. Elastic modulus (a) and hardness (b) on non-used side of railhead as a function of distance from surface.
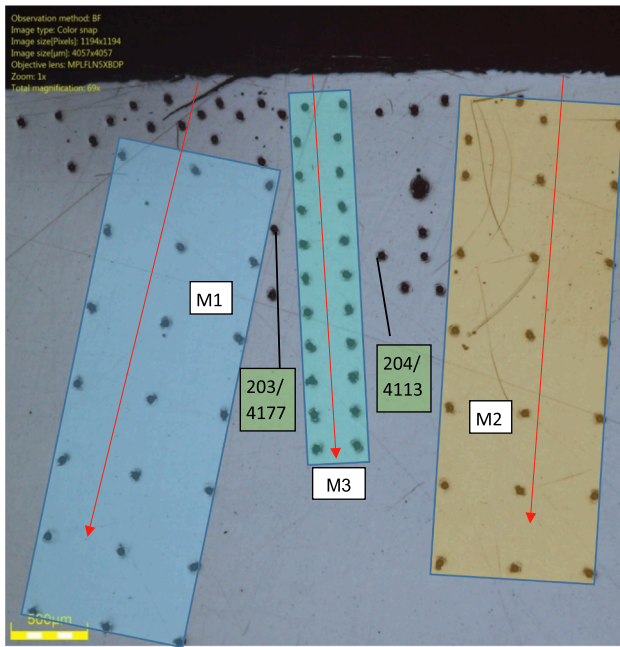

Fig. 4. Location of indents matrices on railhead cross-section, on used side in vicinity of short crack. The values of E/HIT([GPa]/[MPa]) for selected points are shown.

regions.

One important observation is the trace of a crack generated in the railhead. The example of the crack (referred to as the "long crack") is presented in Fig. 10. The crack starts at the railhead surface and goes to the inside of the rail. In general, the cracks are located in region A.

The small area between the long crack and the railhead surface may be considered as part of region A, but inside this area a third kind of microstructure can be seen. This is characterized by fine, elongated grains, deteriorated perlite, and so on, so we refer it as area C. Areas A, B and C are marked in Fig. 10, where the microstructure of the unused side of the rail is also shown. The crack constitutes a sharp boundary between the specific microstructure (area C) and the rest of region A. We can assume that the specific structure above the crack is generated when the crack already exists. The presence of the crack causes a strain discontinuity and enables different deformations of the material above the crack (which constitutes a kind of thin layer), and the bulk of the material below the crack. Therefore, the multi-axial strain resulting from the contact with the wheel may be much greater above the crack than it is below the crack. The greater strain manifests itself as a specific structure in region C. In subsequent load cycles during the lifetime of the rail, the strain difference in the adjacent areas, which are located on different sides of the crack, results in the crack being propagated. The process of the initiation of a crack is still unclear.

The highest hardness is observed in area C, and this area also exhibits the lowest value of the Young modulus. This is a result of the loading history in area C. The direct contact with the wheel and the discontinuity of the strain field due to the presence of the crack allows a quasi-independent deformation of the area above the crack, lead to a relatively large deformation. This results in high strain hardening, which manifests itself as an increase in hardness. On the other hand, the intensive cyclic deformation of this region due to the contact load causes fatigue damage that manifests itself as a serious decrease in the elastic modulus.

Region A (beside and below the crack) is also directly exposed to the contact load, but the deformation in this area is smaller than in area C,
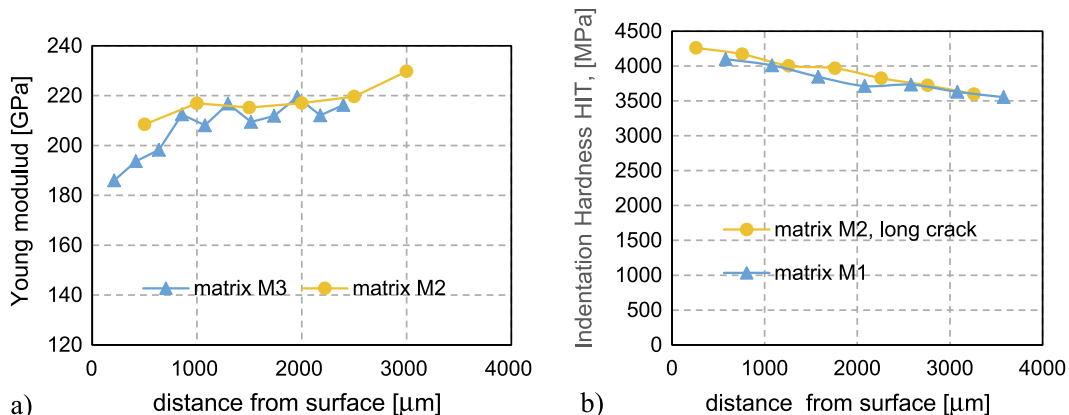

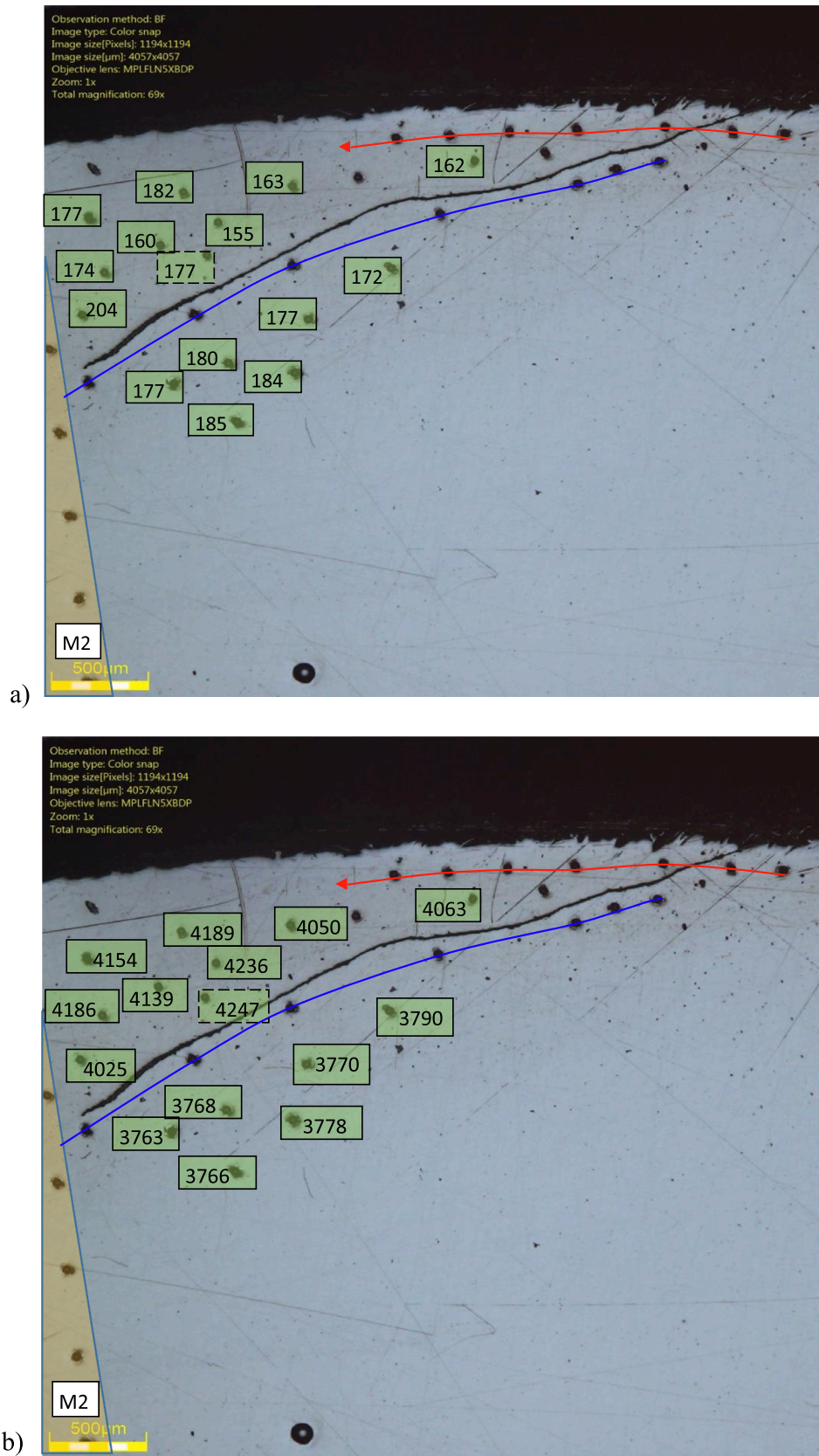**Fig. 5.** Elastic modulus (a) and hardness (b) on used side of railhead as a function of distance from surface.

S. Kucharski et al.

Fig. 6. Elastic modulus (*E*), [GPa] (a), and hardness (*HIT*), [MPa] (b), on used side of railhead in a vicinity of long crack.
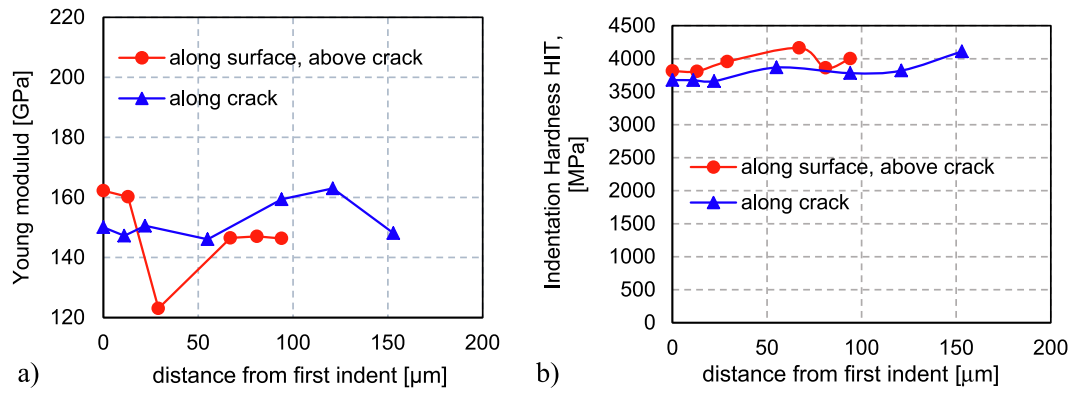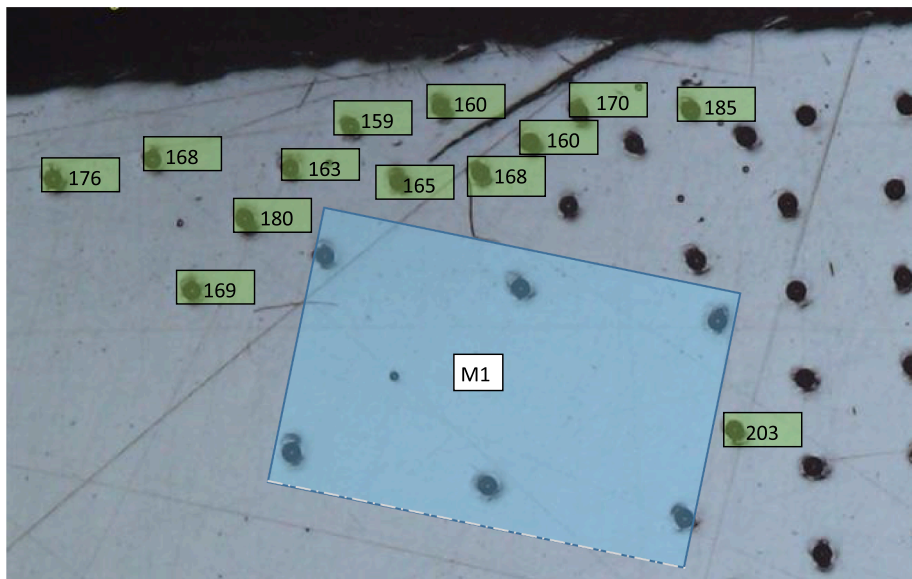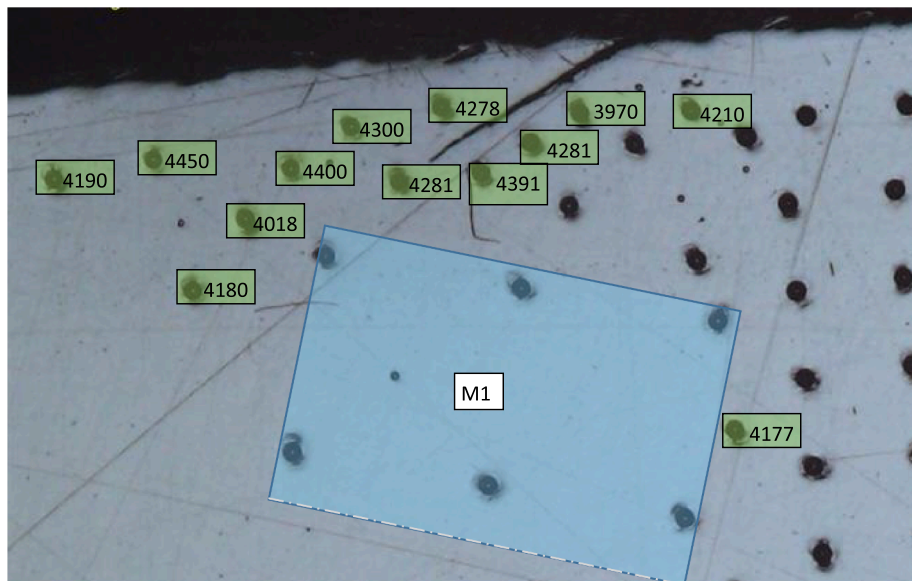
Fig. 7. Elastic modulus (a) and hardness (*HIT*), (b) on used side of railhead along a crack and along a boundary.

a)

b)

Fig. 8. Elastic modulus (*E*), [GPa] (a), and hardness (HIT) [MPa] (b) on used side of railhead in a vicinity of short crack. A part of matrix M1 is also visible.
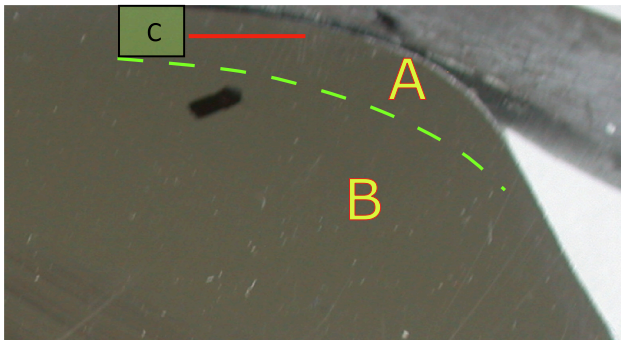
Fig. 9. Regions with different microstructure marked on used side of railhead.

since A is "gripped" by the adjacent part of the rail. Consequently, in region A the hardness values are higher than in the unused side of the rail but lower than in area C. The decrease in the elastic modulus in A is not so important as in region C. This signifies that fatigue damage is not so advanced in this region.

In contrast to the position for the long crack, there is practically no difference in the hardness and elastic modulus between the regions above and below the short crack (Fig. 8). The values of *HIT* and *E* are similar to the values measured at other points near the surface of the

used side of the railhead, such as on the diagrams for matrices M2 and M3 (Fig. 5). The short crack therefore does not constitute a boundary between regions with different deformation modes and different fatigue damage.

3.2.2. Microstructure characterization through the use of scanning electron microscopy (SEM)

We performed an evaluation of the microstructure using a combination of a scanning electron microscope (SEM) on two specimens: a reference specimen without any mechanical load, and a specimen of rail that had been used by railway wheels. The specimens were obtained by cutting and slicing the rail specimens with a slow speed diamond saw. The specimens, measuring 8x8x2 mm, were lapped and polished using a special procedure for SEM specimens. A carbon conductive strip was applied to improve the conductive properties. The specimens were thoroughly examined using JEOL JSM-6380 LA SEM-EDX in a high vacuum. A voltage of 20 kV and an aperture of 120 μm were used, whereas the working distance was 10 mm. The observations were made using a magnification range of 100× to 10000×, but the best results were obtained with the 5000× set-up. Fig. 11 presents the regular lamellar microstructure of pearlitic steel observed in the unused sample.

Dark-coloured fine cementite laths of approximately 200 nm width can be seen here. The interlamellar ferrite spacing is 2–4 times thicker than the ferrite laths itself. The results of a massive plastic deformation
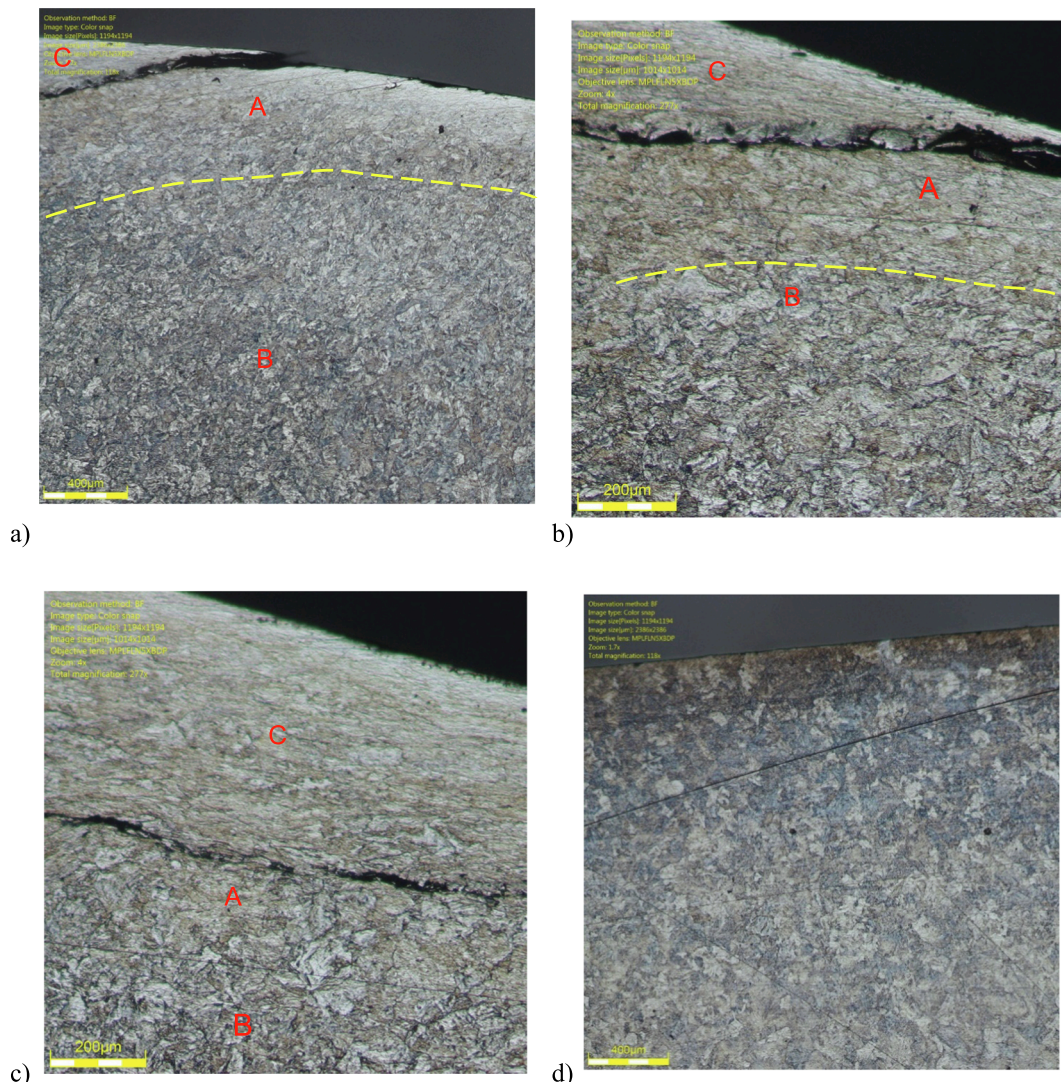

Fig. 10. Microstructure of railhead: a), b), c) - different regions on used side, d) unused side.
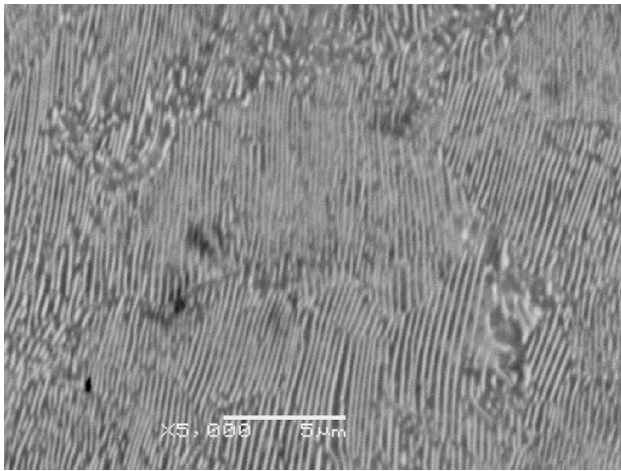
Fig. 11. SEM micrograph made in unused side of investigated sample of the railhead.

can be seen in Fig. 12, which presents the used side of the rail. On the left side of Fig. 12, grains with regular lamellae can be seen. However the right side of the micrograph presents a highly deformed microstructure. The interlamellar spacings are broken and twisted in random directions. The boundaries between the regular and irregular areas are regions that are vulnerable to crack formation processes.

3.3. Cyclic indentation: Estimations of fatigue damage of railhead

The indentation test provides some information about the fatigue damage of the material. The first sign of this damage is the deterioration of the Young modulus. The damage parameter, D, formulated in the framework of Continuum Damage Mechanics (CDM), increases when the elastic modulus decreases:

$$D = 1 - \left(\frac{E_f}{E_0}\right)^{\frac{1}{p}} \quad (2)$$

where E_0 and E_f correspond to the initial state and the final (damaged) state, respectively and p is a constant that should be calibrated, (see, for example, [20]). The low values of the elastic modulus in the regions near the surface of the used side of the railhead indicate that local fatigue damage is taking place. The damage parameter takes its greatest value in region C.

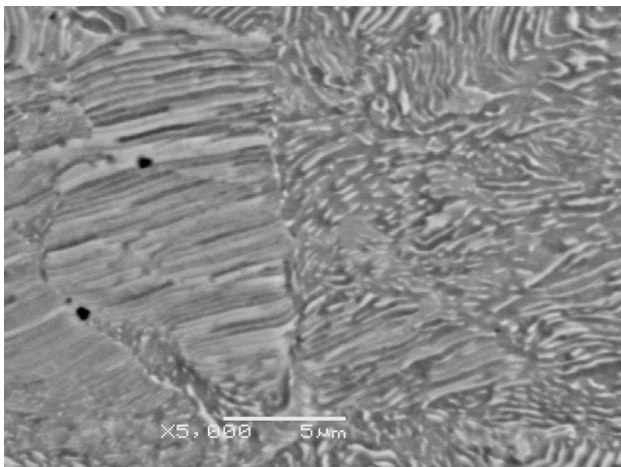An estimation of fatigue damage can be also performed on the basis

Fig. 12. SEM micrograph made in used side of investigated sample of the railhead.

of a cyclic indentation test. The cyclic indentation is controlled by loading and the loading-unloading procedure is repeated 10 times in a fixed location. The evolution of loading force in time is presented in Fig. 13a. The change of P versus time is the same for all cycles, however in the first cycle we have the greatest penetration depth (and largest hysteresis loop), since it starts in the initial state of material, on flat surface. For subsequent cycles the penetration depth is smaller, because the indentation test is carried out in the residual imprint of the previous cycle, so that the surface is no longer flat and this also results in local hardening of the material. Consequently, the hysteresis loops are thinner than in the first cycle.

Although the stress state in the indentation is much more complex than in a uni-axial tensile-compression test, in both tests an evolution of hysteresis loops can be observed. On the basis of a cyclic indentation test, so-called short-time procedures (e.g. [21,22]) can be carried out that enable the fatigue properties of materials, in particular the so-called hardening potential, which correlates with fatigue strength, to be determined. In the frame of this procedure, a 10-cycle indentation test is performed. The evolution of the width of the indentation hysteresis loop h^i_{ap} with the number of cycles, Fig. 13, is correlated with the Woehler curve determined in a uni-axial test (R = −1) for thousands of cycles. The absolute value of h^i_{ap} decreases with the number of cycles i. The greater the reduction of h^i_{ap}, the greater the fatigue strength of the material.

In our paper we propose a similar approach. However, instead of the width of the hysteresis loop, h^i_{ap}, we analyse the evolution of the loop area, which is strictly correlated with h^i_{ap}, and corresponds to the plastic work W_p executed in the loading–unloading cycle. In the indentation test a mechanical work is executed by loading force, that can be calculated as the area below P-h curve, Fig. 13b. In the loading-unloading cycle the difference between work executed during loading and unloading is equal to the energy dissipated into the material during the test and this energy we call the irreversible, plastic work, W^i_p. It can be calculated as the area of the hysteresis loop.

In order to estimate (qualitatively rather than quantitatively) the fatigue resistance of the different regions of the railhead, we performed a cyclic micro-indentation test (10 cycles). The *P-h* curves for the whole test for the used and the unused regions are presented in Fig. 13c. In Fig. 13d, the loops for the second, sixth and tenth cycles are shown. The width of the last of these is distinctly lower than that of the first two, so the decrease in h^i_{ap} and consequently the change in W^i_p is visible.

In Fig. 14 the change in the plastic work W^i_p with the number of cycles is presented for the different railhead regions. An evident difference between the different regions of the railhead can be observed. The smaller decrease of W^i_p with i for the used side than for the unused side, Fig. 14a, indicates that the former exhibits lower fatigue resistance. This may be explained by its loading history, which has multicycles of contact load with the wheel. Fig. 14b shows the evolution of W^i_p in the vicinity of the long crack, in regions C and A marked in Fig. 12. In the latter, W^i_p diminishes much faster than in the former. This indicates that the fatigue resistance of the region above the crack is much lower than the resistance below the crack.

This confirms the hypothesis that region C is subjected to the most intensive fatigue, which is manifested by the most deteriorated microstructure. The highest fatigue damage in region C was also confirmed by the lowest value for the elastic modulus.

3.4. Ultrasonic determination of distribution of Young modulus on a cross-section of the railhead

It is well known that the microstructure of steel under the wheels undergoes severe changes during service, due to plastic deformation and temperature rises caused by the cyclic wheel–rail contacts. These effects are commonly described as the formation of a White Etching Layer (WEL), a Brown Etching Layer (BEL) and a deformed pearlite layer below the wheel–rail contact surface. The microstructural
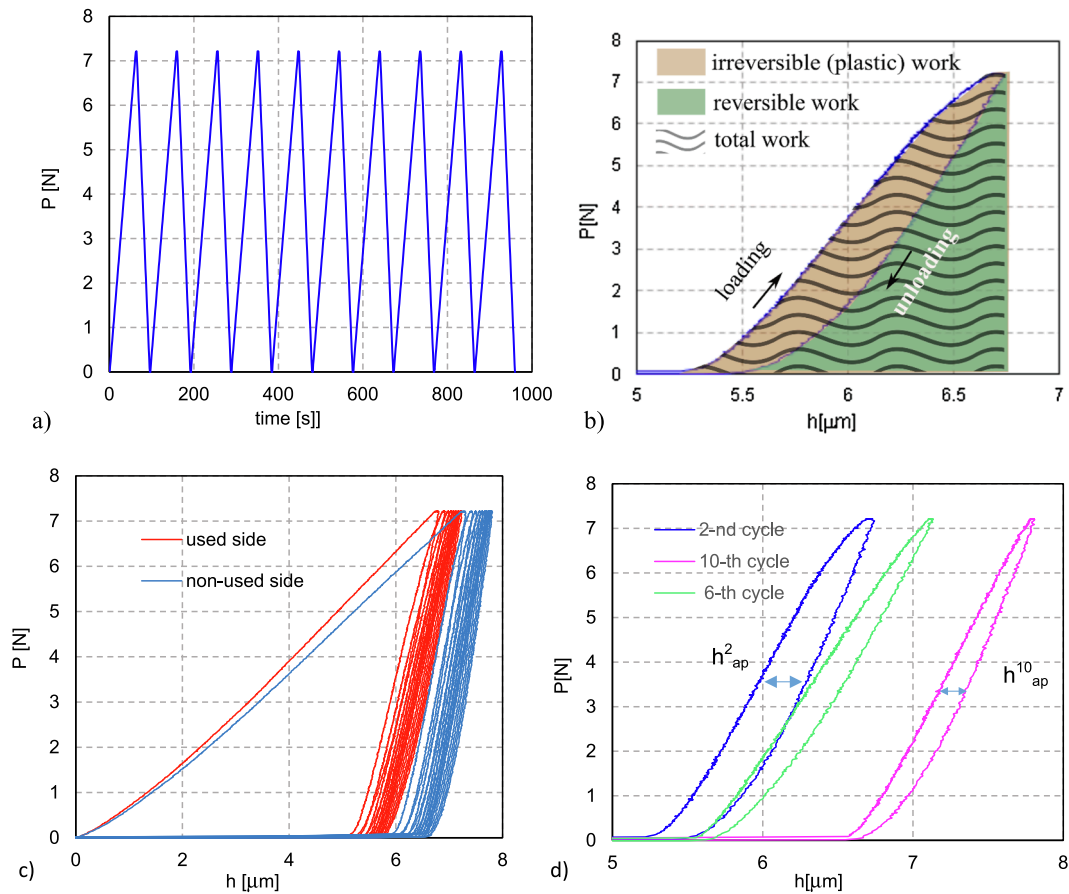
Fig. 13. Cyclic indenation test a) loading versus time, b) reversible and irreversible (plastic) work executed by external force during loading-unloading cycle c) P-h curves for cyclic (loading-unloading) indentation tests of used and non-used area of railhead. The smaller residual penetration depth and lower inclination angle of unloading curves for the used side indicate, respectively, a higher hardness and lower elastic modulus d) the second, sixth and last loop of 10 cycles test for used side.
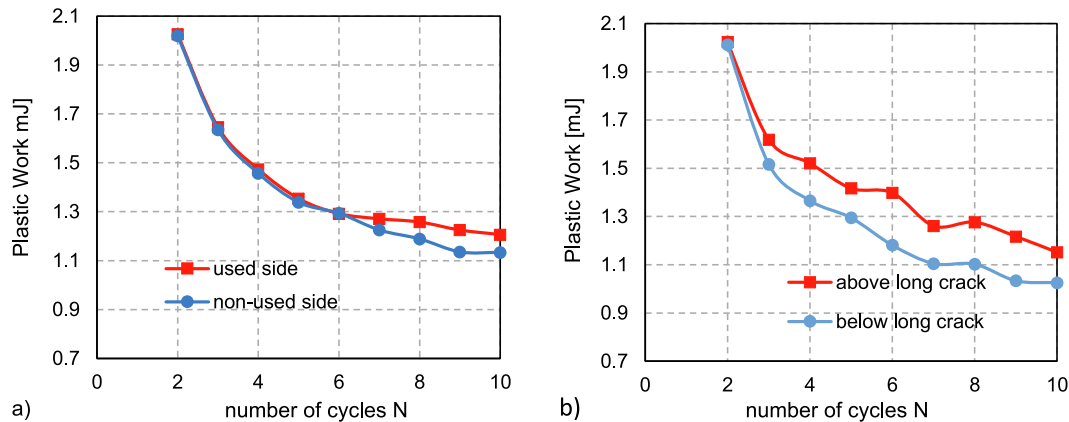

Fig. 14. Evolution of plastic work in subsequent loading-unloading cycles: a) for used and nonused region of railhead, b) for used railhead above and below the crack.

characteristics and formation mechanisms of these layers have been intensively investigated and are comprehensively described (e.g. by Kumar *et al.* [7]. The important result of these studies is that the thickness of the WEL in straight tracks is typically 25–40 µm and in curved track sections rises to 100–120 µm. Also, from the theoretical modelling of the stress and temperature distribution below the wheel–rail contact it follows that the rail steel deforms plastically up to a depth of about 200 µm under the contact surface [8]. Generally, it can be said that the depth of rail material directly affected by the wheel–rail contact can be estimated as a fraction of a millimetre, but that regions

located further down are also affected by the stresses mentioned above.

The bulk of the railhead material sustains considerable loading during each wheel–rail contact cycle. Such repeating loadings, even below the yield strength of the material, can cause certain changes in the dislocation structure within the material grains and on the grain boundaries. The possible changes in dislocation density and mobility can become manifest on the macroscopic level as small but measurable changes in the elastic moduli of the affected rail material. It can also be predicted that the deviations in elastic moduli from the initial state should be most pronounced in the areas of maximal stress concentration,

which are located under the wheel–rail contact area on the gauge (i.e. inner) side of the railhead, as well as on the head–neck transition zone.

To investigate this possibility experimentally, we performed ultrasonic measurements of the distribution of the Young modulus on a cross section of railhead cut out from the heavily used rail with a significantly worn profile (Fig. 1a). The thickness of the cut section was about 5 mm.

The measurements of the Young modulus were performed along three horizontal lines situated in the upper, middle and lower part of the railhead cross-section (Fig. 1a). On each measurement line there were several measurement points distributed every 5 mm from the field to the gauge (i.e. inner) side of the railhead section.

The elastic properties of materials can be effectively determined by the ultrasonic method on the basis of measurements of the velocities of ultrasonic waves propagating in the investigated material. The number of elastic constants of the material, as well as the ultrasonic methodology used for their determination, depends on the material's elastic symmetry [23]. In the present case we examined hot rolled pearlitic steel, which exhibits isotropic symmetry. Such a material can be characterized by two independent elastic constants – for example, the Young modulus E and Poisson's ratio ν. Any other elastic constants, such as the bulk modulus K or the shear modulus G, can be directly calculated from the first two using the well-known elasticity relations.

To determine the two elastic constants of an isotropic material, two ultrasonic velocities have to be measured, namely the velocity of the longitudinal wave V_L and the velocity of the transversal wave V_T. From the elastic waves theory [24], the two following expressions for the elastic moduli of an isotropic material, E and ν, can be deduced:

$$E = \rho \frac{(3V_L^2 V_T^2 - 4V_T^4)}{(V_L^2 - V_T^2)} \qquad (3)$$

$$\nu = \frac{(\frac{1}{2}V_L^2 - V_T^2)}{(V_L^2 - V_T^2)} \qquad (4)$$

where: ρ - mass density

V_L – velocity of longitudinal ultrasonic waves,
V_T – velocity of transversal ultrasonic waves.

For the measurements of the ultrasonic velocities in the railhead sample, the pulse-echo contact technique was used (see Fig. 15). In this commonly used technique, a short pulse of ultrasonic energy is introduced to the sample by an ultrasonic probe coupled to the surface. The pulse undergoes multiple reflections between the sample faces, producing successive ultrasonic echoes that are detected by the probe and displayed on the screen of the ultrasonic apparatus (see Fig. 16).

The time-of-flight difference between two successive echoes is exactly the time taken by the ultrasonic pulse to pass back and forth through the sample thickness. The ultrasonic wave velocity V can therefore be calculated from the formula:

$$V = \frac{2\,L}{\Delta t_{1-2}} \qquad (5)$$

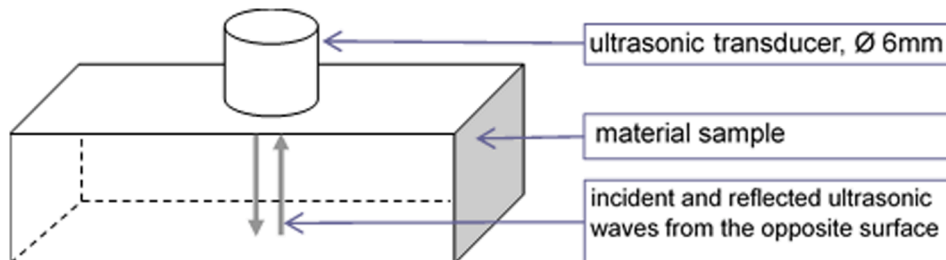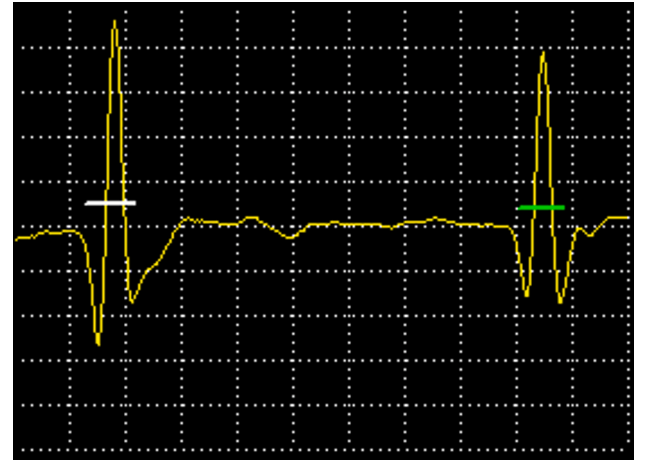where: L – thickness of the tested sample at the measurement point

Fig. 16. Waveforms of two echoes obtained using 10 MHz longitudinal waves transducer. The difference of time-of-flight between 1-st and 2-nd echo is measured exactly between the zero crossing points of relevant pulses.

Δt_{1-2} – time difference between 1-st and 2-nd multiple echo.

The same measurement configuration was used when longitudinal and transversal waves were propagating within the bulk of the material. For the generation of the longitudinal waves a transducer with a nominal frequency of 10 MHz was used, whereas for the transversal waves a transducer with a nominal frequency of 5 MHz was selected. In both cases the transducer diameter was about 6 mm. This means that the measurement results obtained for every measurement point actually represent the average value for the material cylinder of 6 mm diameter located directly under the measuring transducer.

The ultrasonic measurement system consisted of a Panametrics Epoch 4 ultrasonic flaw detector remotely controlled by a PC with proprietary software for the accurate measurement of the time-of-flight of ultrasonic pulses. To provide the acoustic coupling between the ultrasonic transducers and the specimen surface, glycerine was used in the case of the generation of longitudinal waves and high viscosity resin otherwise. Taking into consideration the fact that the thickness of the measured sample L was measured with an accuracy of ± 0.01 mm and the time-of-flight difference Δt_{1-2} with an accuracy of ± 0.005 μs, we estimated that the resulting accuracy of the determination of the longitudinal wave velocity was about ± 30 m/s and of the transversal wave velocity ± 10 m/s. Considering formula (5) we finally conclude that the accuracy of determination of the Young modulus on the sample of railhead under examination was about ± 1.5 GPa, which is about 0.7% of the measured values. This is a relatively high accuracy that can detect even minor changes in the material condition.

The measurement results are illustrated in Figs. 17, 18, and 19, separately for each of the three measurement lines. The highest values of the Young modulus (213.5 GPa) were measured on the upper line near the gauge corner of the railhead, where the rail stresses due to the wheel–rail contact are the highest. These values are about 4.5 GPa
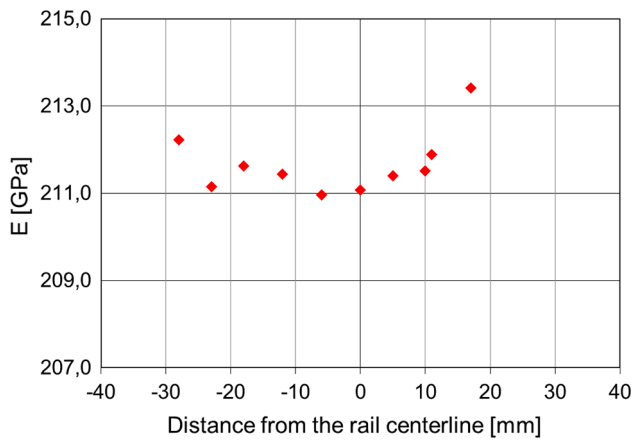

Fig. 15. Schema of measurements of ultrasonic wave velocities in material sample with pulse-echo technique.

Fig. 17. Diagram illustrating Young's modulus for the upper line, *vide* Fig. 1a.
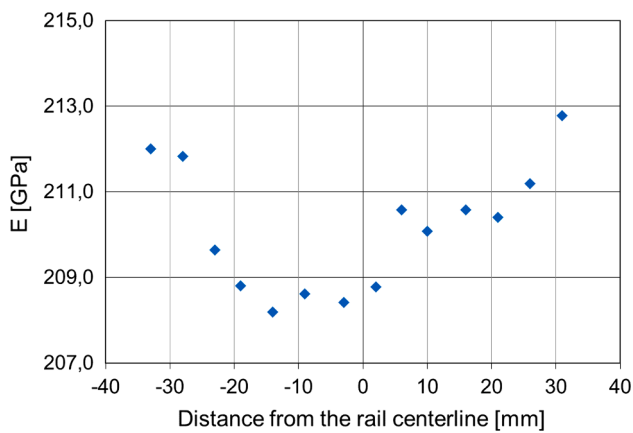

Fig. 18. Diagram illustrating Young's modulus for the middle line, *vide* Fig. 1a.
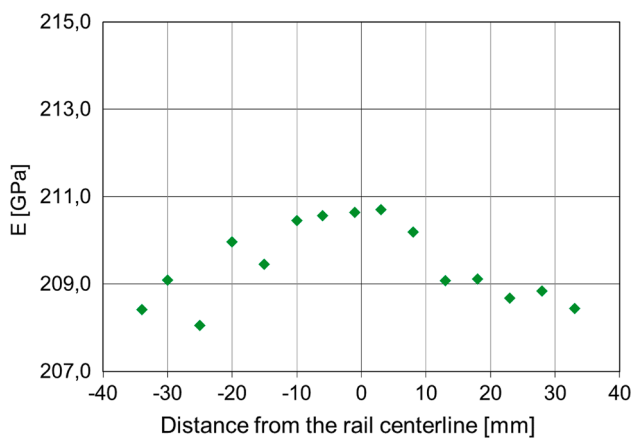

Fig. 19. Diagram illustrating Young's modulus for the bottom line, *vide* Fig. 1a.

higher than the values measured on the lower measurement line at the same distance from the rail centre line, where the rail stresses are the lowest. On the middle line, the Young modulus also has its highest values near the gauge corner, but they are considerably lower (at the same transversal position) than on the upper line, and higher than on the lower line. This suggests that the Young modulus rises with the cumulative load transferred by the material during service. This interpretation is confirmed by the distribution of the Young modulus on the lower measurement line (Fig. 19). This time the highest values (210.7 GPa) are registered near the rail centre line, not near the rail sides. This can be

explained by the fact that the stress concentrates above the rail neck, which takes the full load exerted by the wheels on the railhead. A similar result concerning the stress concentration during wheel–rail contact is described in paper [23], in which the von Mises stress distribution obtained from the solution of a three-dimensional finite element model is shown.

This interesting interpretation of the results we obtained is somewhat contradicted by the distribution of the Young modulus on the middle measurement line (Fig. 18). This is because the Young modulus rises considerably not only near the gauge corner of the railhead but also near the field corner, where the load stresses should be small. However, we do not know the history of the service life of the tested rail, so it is difficult to draw a firm conclusion concerning this result. It is possible that the tested rail was moved during service from one side of the railway track to the other, and the modulus rise on the apparent field side may be a reminder of its former service with the sides flipped.

Despite the doubts related to the interpretation of the results we obtained, it is indisputable that the values of the Young modulus measured on the cross-section of the used railhead change from about 208 GPa near the lower corners of the head to about 213.5 GPa near the upper gauge corner of the head. This difference is considerably greater than the measurement error of the ultrasonic technique that we applied (± 1.5 GPa) and means that the true reason for the changes detected in the Young modulus are real differences in the condition of the material in the different parts of the railhead cross-section.

To confirm our preliminary interpretation that the main reason for the observed changes in the Young modulus distribution are the differences in cumulative load transferred by different parts of the railhead, it would be necessary to perform similar experiments on more samples cut out from rails at different stages of service life as well as from brand new rails. The measurements performed on brand new rails could exclude or confirm the concept that the non-homogeneous distribution of the Young modulus on the cross-section of the railhead is caused by technological processes in the production of the rails. On the other hand, measurements performed on rails on different stages of their service life could exhibit some correlation between changes in the Young modulus in certain parts of the railhead cross-section and the cumulative load transferred by the rail during service life.

4. Conclusions

The change in the mechanical properties and microstructure of a railhead due to the cyclic contact load with the wheel was investigated. The unused side of the same rail was taken as a reference.

Both the mechanical properties and the microstructural analysis show that on the used side of the railhead the material is not homogeneous and some characteristic regions can be distinguished. The difference between the different regions results from the manufacturing processes and contact loads that occur in service life. The tests at the macro scale (Brinell hardness and ultrasonic measurements) that cannot be conducted very close to the railhead surface enabled us to capture the effects of manufacturing technology: a moderate increase in the Brinell hardness and a small increase in the elastic modulus were observed in both the used and the unused, outer, side of the railhead (see Figs. 1, 17). The measurements in the vicinity of the rail surface were generally greater than those registered in the bulk material. Regarding the macro scale measurements the difference in Brinell hardness and *E* between the used and the unused side was rather low.

A micro-indentation test was applied to examine the regions of the railhead located closer to the rail surface, and to detect local changes resulting from the cyclic contact load during service life. The influence of cracks on the evolution of local material properties was also analysed. It was found that the adjacent regions above and below a crack have different microstructures, hardness and elastic moduli. In these regions there is therefore a difference in strains resulting from the contact load. This may be a cause of crack propagation.

It was shown that in the near-surface zone on the used side, the hardness increases by approximately 10% and the elastic modulus decreases by 18% when compared with the values determined on the virgin side, and the highest hardness values and the lowest elastic modulus values occur in the area between a crack and the railhead surface.

The results of the ultrasound velocity tests revealed that the values of the Young modulus measured using these tests on the cross-section of the used railhead changed from about 208 GPa near the lower corners of the railhead to about 213.5 GPa near the upper head surface that was in contact with the train wheel. This difference was greater than the measurement error of the technique that was applied (± 1.5 GPa).

Two approaches were followed to estimate the local fatigue damage of the material in the near surface zones. In the first, the decrease in the elastic modulus on the used side was analysed. The second approach was based on the cyclic indentation test. The evolution of the plastic work executed in subsequent cycles was compared for the used and unused sides of the railhead. Both methods indicated that local fatigue strength in the near surface zones on the used side was lower than the strength on the unused side. Our estimation has a qualitative rather than a quantitative character. Rails with a known service life history should be examined to calibrate some of the parameters to enable quantitative results to be obtained, and to predict the fatigue life of a partially used railhead.

Declaration of Competing Interest

The authors declare that they have no known competing financial interests or personal relationships that could have appeared to influence the work reported in this paper.

Data availability

Data will be made available on request.

References

[1] Herian J, Aniolek K. Modelling of structure and properties of pearlitic steel and abrasive wear of the turnout frog in the cyclic loading conditions. J Achieve Mater Manuf Eng 2011;49:71–81.

[2] Kazeminezhad M, Taheri AK. The effect of controlled cooling after hot rolling on the mechanical properties of a commercial high carbon steel wire rod. Mater Des 2003;24:415–21.

[3] Dollar M, Bernstein IM, Thompson AW. Influence of deformation substructure on flow and fracture of fully pearlitic steel. Acta Metall 1988;36(2):311–20.

[4] Kuziak R, Pidvysots'kyy V, Rauch Ł, Pietrzyk M, Zygmunt T. Method for heat treatment of the running surface of the head of the pear-litic steel rails. J Metal Mater 2021;73(1):9–15.

[5] Clayton P, and. Allery MBP. Metallurgical aspects of surface damage problems in rails. Canadian Metallurgical Quarterly 1982; 21: I, 31-46.

[6] Bhavani G, Srivastava PJ, Mahesh V. Characterization of used and virgin pearlitic rail steel. Mater Today: Proc 2021;39:454–8.

[7] Kumar A, Agarwal G, Petrov R, Goto S, Sietsma J, Herbig M. Microstructural evolution of white and brown etching layers in pearlitic rail steels. Acta Mater 2019;171:48–64.

[8] Srivastava JP, Sarkar PK, Kiran MVR, Ranjan V. A numerical study on effects of friction-induced thermal load for rail under varied wheel slip conditions. Simul Trans Soc Model Simul Int 2018;95:351–62.

[9] Bjørheim F, Siriwardane SC, Pavlou D. A review of fatigue damage detection and measurement techniques. Int J Fatigue 2022;154(106556):1–15.

[10] Pavlou DG. Prediction of Fatigue Damage Accumulation under Real Loading Spectra. University of Patras; 1994.

[11] Ye DY, Wang DJ, An P. Characteristics of the change in the surface microhardness during high cycle fatigue damage. Mater Chem Phys 1996;44(2):179–81.

[12] Ye D, Tong X, Yao L, Yin X. Fatigue hardening/softening behaviour investigated through Vickers microhardness measurement during high-cycle fatigue. Mater Chem Phys 1998;56(3):199–204.

[13] Pavlou DG. A phenomenological fatigue damage accumulation rule based on hardness increasing, for the 2024–T42 aluminum. Eng Struct 2002;24(11):1363–8.

[14] Ye D, Wang Z. Approach to investigate pre-nucleation fatigue damage of cyclically loaded metals using Vickers microhardness tests. Int J Fatigue 2001;23(1):85–91.

[15] Drumond G, Roudet F, Chicot D, Pinheiro B, Pasqualino I. A damage criterion to predictthe fatigue life of steel pipelines based on indentation measurements. J Offshore Mech Arct Eng 2021; 143 (1) 011701 (10 pages).

[16] Miroslav Š, Vladimír C, Kepka M. Possibility of fatigue damage detection by non-destructive measurement of the surface hardness. Procedia Struct Integrity 2017;7: 262–7.

[17] Nagy PB. Fatigue damage assessment by nonlinear ultrasonic materials characterization. Ultrasonics 1998;36(1–5):375–81.

[18] Oruganti R, Sivaramanivas R, Karthik T, Kommareddy V, Ramadurai B, Ganesan B, et al. Quantification of fatigue damage accumulation using non-linear ultrasound measurements. Int J Fatigue 2007;29(9-11):2032–9.

[19] Kenderian S, Berndt TP, Green Jr RE, Djordjevic BB. Ultrasonic monitoring of dislocations during fatigue of pearlitic rail steel. Mater Sci Eng A 2003;348(1–2): 90–9.

[20] Ustrzycka A, Mróz Z, Kowalewski ZL, Kucharski S. Analysis of fatigue crack initiation in cyclic microplasticity regime. Int J Fatigue 2019;1:1–15.

[21] Ostermayer P, Ankener W, Blinn B, Smaga M, Eifler D, Beck T. Analysis of the Subsurface Volume of Differently Finished AISI 52100 by Cyclic Indentation and X-Ray Diffraction. Steel Research Int 2021;92(2100253):1–11.

[22] Kramer HS, Starke P, Klein M, Eifler D. Cyclic hardness test PHYBAL$_{CHT}$ - Short-time procedure to evaluate fatigue properties of metallic materials. Int J Fatigue 2014;63:78–84.

[23] Srivastava JP, Sarkar PK, Ranjan V. Contact Stress Analysis in Wheel-Rail by Hertzian Method and Finite Element Method. Journal of The Institution of Engineers (India) 2014;95:319–25.

[24] Auld BA. Acoustic Fields and Waves in Solids. New York, London, Sydney, Toronto: John Wiley & Sons; 1973.